JGR Atmospheres

RESEARCH ARTICLE

10.1029/2025JD045282

Can Large-Scale Clustering of Tropical Precipitation Be Used to Constrain Climate Sensitivity?

P. Blackberg[1,2] **and M. S. Singh**[1,2]

[1]School of Earth, Atmosphere, and Environment, Monash University, Clayton, VIC, Australia, [2]Centre of Excellence for the Weather of the 21st Century, Monash University, Clayton, VIC, Australia

Key Points:

- Climate models project future increases in large-scale clustering of tropical precipitation and a meridional contraction of heavy rainfall
- Changes in clustering are sensitive to the Pacific SST gradient in observed and simulated interannual variability and in model projections
- Effect of changes in clustering on the radiation budget depends on timescale, precluding an observational constraint on climate sensitivity

Supporting Information:

Supporting Information may be found in the online version of this article.

Correspondence to:

P. Blackberg,
carlphiliposcar@gmail.com

Citation:

Blackberg, P., & Singh, M. S. (2026). Can large-scale clustering of tropical precipitation be used to constrain climate sensitivity? *Journal of Geophysical Research: Atmospheres*, *131*, e2025JD045282. https://doi.org/10.1029/2025JD045282

Received 6 SEP 2025
Accepted 1 APR 2026

Author Contributions:

Conceptualization: P. Blackberg, M. S. Singh
Formal analysis: P. Blackberg
Funding acquisition: M. S. Singh
Investigation: P. Blackberg
Methodology: P. Blackberg, M. S. Singh
Project administration: M. S. Singh
Supervision: M. S. Singh
Visualization: P. Blackberg
Writing – original draft: P. Blackberg
Writing – review & editing: M. S. Singh

Abstract

The spatial organization of deep convection in tropical regions is posited to play an important role in determining characteristics of the tropical climate such as the humidity distribution and cloudiness and may therefore be an important control on climate feedbacks. This study analyzes one aspect of convective organization, the clustering of heavy precipitation on large scales, in both interannual variability and under warming in future climate projections. Clustering is quantified by the total areal coverage and mean size of precipitation features exceeding a climate-dependent threshold. Both observations and global climate models (GCMs) suggest increased clustering under El Niño conditions, but the relationship of this clustering to the tropical humidity and cloud distribution differs in different GCMs. Under future warming, all models considered project an increase in clustering associated with a narrowing of the intertropical convergence zone and with a model-spread partially explained by differences in projections of the Pacific SST gradient ($r = -0.46$). However, unlike in interannual variability, a general spatial clustering with warming do not explain the climatological humidity or low-cloud responses, limiting a simple observational constraint on feedbacks. Notably, a few model outliers drive considerable spread in tropical-mean mid-tropospheric drying, which appears to be partially linked to clustering of heavy rainfall meridionally toward the equator. These results suggest possible future targets for model evaluation.

Plain Language Summary

The spatial distribution of rainfall in the tropics is expected to change in a warming climate, with potentially important impacts on how much radiation is absorbed by water vapor and reflected by clouds. This study shows that heavy rainfall tends to move towards the equator and to the Pacific Ocean in projections with global climate models, resulting in an overall increase in the "clustering" of rainfall on the large scale. Further, the results show a shift in rainfall to the equator with global warming is associated with a drying of the tropical atmosphere, which may have an influence on how much the planet warms for a given CO_2 change. However, similar observed shifts in rainfall in the current climate are not found to have the same effect on humidity and clouds as for changes with warming, suggesting caution should be exercised when using relationships derived from observations to predict future changes.

1. Introduction

The spatial organization of deep convection in tropical regions plays a critical role in shaping the hydrological cycle and the moisture and cloud distribution (Hartmann et al., 1984). Changes in organization with warming may therefore have implications for a range of climatic processes, including precipitation extremes (e.g., Bao et al., 2017; Pendergrass et al., 2016; Semie & Bony, 2020) and the radiative feedbacks that control equilibrium climate sensitivity (ECS) (e.g., Bony et al., 2020; Emanuel et al., 2014; Schiro et al., 2022). However, because many of the relevant small-scale processes are not resolved in climate models, it remains unclear how convective organization will evolve in a warmer climate.

While there are numerous ways by which convection may organize, one important mechanism is the clumping or clustering together of convective elements (e.g., Bretherton et al., 2005; Maddox, 1980; Mapes, 1993). Such clustering occurs on a range of scales (Mapes & Houze, 1993), including at large scales that are resolved by climate models and at mesoscales that can typically only be resolved in high-resolution storm-resolving simulations. Recently, Bläckberg and Singh (2022) showed that the extent to which tropical precipitation exhibits clustering on the large scale increases with warming in climate projections from the Coupled Model Intercomparison Project phase 5 (CMIP5). This large-scale clustering is distinct from other types of organization on the mesoscale, but idealized simulations suggest that similar processes may act at both scales, and that both large-scale and mesoscale organization of convection may modulate the radiation budget (Wing et al., 2018).

Here we build on the work of Bläckberg and Singh (2022), showing that increased clustering of heavy precipitation with warming is a robust feature of the more recent CMIP6 as well as CMIP5. Further, we explore the mechanisms that lead to large-scale clustering of precipitation in the tropics and the influence of an increase in clustering on properties of the atmosphere that are important for the radiation budget. The analysis will compare how clustering varies across different timescales, from interannual variability in both models and observations to changes in the climatological clustering of convection in a warming climate. This approach allows us to assess whether observational constraints of convective organization under current climate conditions can help constrain changes in organization and the associated radiative feedbacks with warming.

Previous studies have highlighted observed relationships between convective organization and the tropical radiation budget (Bony et al., 2020; Holloway et al., 2017; Tobin et al., 2013). For example, Bony et al. (2020) find tropical mesoscale convective organization and Estimated Inversion Strength (EIS) in subsidence regions are the two strongest predictors of deseasonalized interannual variability in net top-of-atmosphere radiation, together explaining about 60% of the variance. While the two predictors are significantly correlated and potentially partly mechanistically connected (Williams et al., 2023), the authors find that both have an independent contribution in influencing the tropical radiation budget; EIS is found to have a stronger correlation with the cloudy component of the radiation budget while convective organization is found to have a stronger connection to the clear-sky component of the radiation budget. Bony et al. (2020) argue that clustering of deep convective elements is associated with a tropical-mean drying, resulting in increased outgoing longwave radiation due to a reduction in the greenhouse effect.

This hypothesis is supported by idealized studies of convective “self-aggregation” (e.g., Wing & Emanuel, 2014). Both cloud-resolving and climate-model simulations run in idealized settings reminiscent of tropical conditions (i.e., low rotation rate and weak temperature gradients) show increased outgoing longwave radiation when convection is more clustered within the domain (Wing et al., 2018).

The preceding studies suggest that increased clustering of convection with warming may lead to a negative clear-sky feedback from clustering-induced drying, resulting in reduced equilibrium climate sensitivity (ECS) (Emanuel et al., 2014). However, recent research suggests that clustering of deep convection on the large scale may also be indirectly connected to a positive shortwave feedback on warming through changes in low clouds (Schiro et al., 2022). According to this argument, drying associated with increased clustering of convection is controlled by the large-scale overturning circulation and is most pronounced in regions of climatological descent where low-cloudiness is sensitive to changes in relative humidity. The associated cloud changes then lead to a net positive feedback.

As the above discussion highlights, an important control on convective organization at both large- and mesoscales comes from large-scale circulation patterns, including the Intertropical Convergence Zone (ITCZ), the South Pacific Convergence Zone (SPCZ), the Walker circulation, and convectively coupled tropical waves (Arnold & Randall, 2015; Bony et al., 2020; Quan et al., 2025; Wheeler & Kiladis, 1999; Wodzicki & Rapp, 2016). Changes to the clustering of precipitation under warming may therefore be linked to, for example, a “narrowing” of the ITCZ due to constraints on the export of energy by the Hadley cell (Byrne & Schneider, 2016) or changes in the Walker circulation driven by changes in zonal SST gradients (Quan et al., 2025), which may be associated with “El Niño-like” shifts in the SST climatology (Watanabe et al., 2024).

The existing literature shows that large-scale clustering is projected to increase from the forced response of global warming (e.g., Bläckberg & Singh, 2022; Pendergrass et al., 2016), and that a more clustered state in observed interannual variability, albeit on a different spatial scale, is associated with clear-sky and cloud-radiative feedbacks (Bony et al., 2020). In this study we elucidate to what extent observed and modelled interannual variability in large-scale clustering of heavy precipitation connects to similar radiative feedbacks and whether such relationships can be used to constrain climate sensitivity. To do so, we quantify the relationship between clustering of heavy rainfall and the distribution of relative humidity and low-cloudiness in observations, a high-resolution GCM from the NextGEMS pre-final cycle, and GCMs from the CMIP6 ensemble (method described in Section 2). The results of this study adds to the existing literature by describing the spatial patterns of heavy rainfall that promote large-scale clustering (Section 3), the associated mechanisms involving SST patterns and a

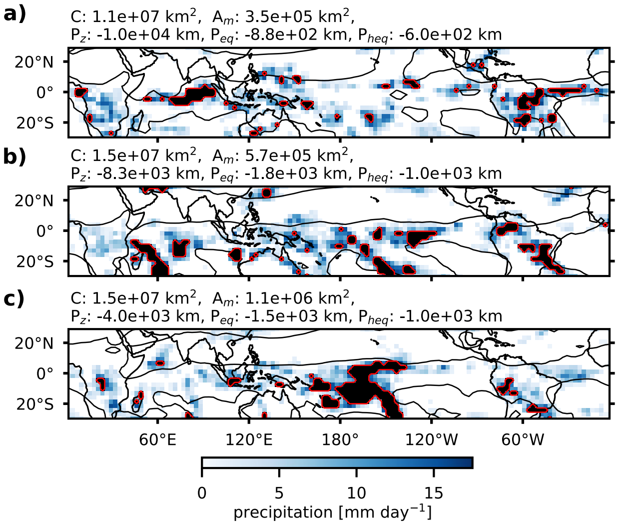

Figure 1. February daily snapshots of GPCP precipitation (blue colors) and heavy precipitation (black shading) features (red contour), with monthly specific humidity representing the median over the tropics (black contour). The panel titles show the total area coverage of heavy precipitation, C, and the mean area of precipitation features, A_m, with the proximity of heavily precipitating points to the central Pacific, equator, and hydrological equator below (described in greater detail in Figure 4).

narrowing of the ITCZ (Section 4), and the tropical radiative feedbacks associated with a more clustered state (Section 5) in interannual variability and for projected climatological changes with warming. Section 6 gives a summary of the key findings and an outlook for future research.

2. Data and Methods

Our analysis is focused on variations in the large-scale clustering of heavy precipitation in the tropics and its relationship to the atmospheric state in both observations and an ensemble of global climate models (GCMs) primarily from CMIP6. We begin by describing the data sets (both model and observational) used, before we describe the quantification of large-scale clustering, and our analysis framework.

2.1. Models

We use simulations from 27 GCMs from CMIP6 (Eyring et al., 2016), using data from the years 1970 to 1999 in the historical scenario, representing the current climate, and from the years 2070 to 2099 under the Shared Socioeconomic Pathway 585 (SSP5-8.5), representing a warmer climate. The models are chosen based on availability of the required variables and we use one ensemble member from each model (see Table S1 in Supporting Information S1 and list in Figure 5).

In addition to the CMIP6 models, we also consider a simulation using a high-resolution GCM referred to here as IFS_9_FESOM_5 (Koldunov et al., 2023). The Deutsches Klimarechenzentrum (DKRZ) Next Generation Earth Modelling Systems (NextGEMS) pre-final cycle provides high-resolution globally simulated atmospheric and oceanic variables for SSP3-7.0 forcing between 2025 and 2049 using the ECMWF Integrated Forecasting System (IFS) at ∼9 km horizontal grid spacing for the atmosphere and the Finite-VolumE Sea Ice-Ocean model version 2 (FESOM2) at 5 km horizontal grid spacing for the ocean (Koldunov et al., 2023). Although the model is at high resolution compared to the CMIP6 models, it retains a convection parameterization, and we therefore describe it as a GCM rather than a storm-resolving model. Because the simulated period is relatively short and the climate change signal during the simulation is small, we only use the high-resolution GCM to characterize interannual variability, using all available years.

2.2. Observations

Observed clustering of tropical precipitation is quantified based on daily precipitation estimates from the National Oceanic and Atmospheric Administration Global Precipitation Climatology Project (NOAA-GPCP) (Huffman et al., 2023), using the method described in the next subsection. We further use NOAA-GlobalTemp (Huang et al., 2024) and Clouds and the Earth's Radiant Energy System (CERES) data (Doelling et al., 2013) to provide observational estimates of surface temperature and top of the atmosphere radiative fluxes, respectively. Estimates of vertical pressure velocity and specific and relative humidity are taken from the fifth generation of the European Centre for Medium-Range Weather Forecasts reanalysis (ERA5) (Hersbach et al., 2023). Apart from precipitation, all variables are taken as monthly averages.

Finally, we develop a simple estimate of the low-cloud fraction using the tropical weather states defined in Tselioudis et al. (2010) based on data from the International Satellite Cloud Climatology Project (ISCCP) (Young et al., 2018). Tselioudis et al. (2010) used a clustering algorithm to categorize histograms of cloud-top pressure and optical thickness given by the ISCCP D1 data set into a series of weather states defined in three hourly polar-orbiting satellite scans with daily global coverage on a $1^\circ \times 1^\circ$ grid. Each weather state is characterized by a histogram in cloud-top pressure and optical thickness that represents the centroid over all members of that weather state. Here we estimate the cloud fraction as a function of pressure for a given weather state as the total frequency of clouds of all optical thicknesses in a given range of cloud-top pressure within the corresponding centroid histogram. We then calculate the low-cloud fraction LCF_i of weather state i as the total cloud fraction below 600 hPa. The monthly low-cloud fraction is taken as

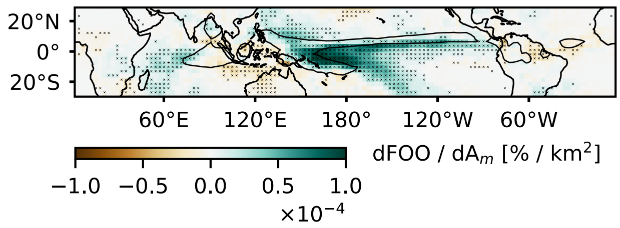

Figure 2. GPCP frequency of occurrence of heavy precipitation, FOO, regressed onto the mean area of heavy precipitation features, A_m, for interannual variability. The contour shows the 90th percentile of the climatological FOO and crosses indicate whether correlations are statistically significant.

$$LCF = \sum_i f_i LCF_i, \tag{1}$$

where f_i is the frequency of weather state i over the month in question.

As described further below, all observational data sets are regridded conservatively to a common 2.8° × 2.8° grid for analysis. We use observations covering the time period between 1998 and 2023 for all data sets, except for cloud fraction (based on ISCCP), which is limited to 1998–2017.

2.3. Quantifying Large-Scale Clustering of Heavy Precipitation

We quantify clustering of precipitation following Bläckberg and Singh (2022) using daily surface precipitation in the tropics (30°S–30°N). To facilitate the comparison of clustering across different models and the observations, we first interpolate the daily precipitation to a 2.8° × 2.8° grid using a first-order conservative method (Jones, 1999) to preserve tropical-mean properties from the native grid. Next, we define heavily precipitating regions as gridboxes for which the precipitation rate exceeds a threshold. The threshold is calculated as the 95th spatial percentile of daily precipitation over all gridboxes in the tropics temporally averaged over the 30-year climatology (or 25-year in the case of observations and the high-resolution model). For the GPCP observations, this threshold is 16 mm day^{-1} and in models the interquartile range in thresholds is 15–17 mm day^{-1}. Distinct heavy precipitation features are identified as 8-connected contiguous regions of precipitation exceeding the threshold or single grid boxes if there are no neighboring connections. While there are conceptual differences in what type of rainfall that is represented by different percentile thresholds, overall conclusions of the paper are not sensitive to using the 90th, 95th, or 97th percentile.

We define our primary measure of clustering, A_m, as the mean area of heavy precipitation features over the entire tropics. A_m conceptually captures clustering by distinguishing scenes with many small precipitation features and scenes where precipitation is aggregated into fewer and/or larger precipitating features (Figures 1 and 3c). The mean area of features, A_m, was chosen due to its interpretability, however, we note that it is only one aspect of the large-scale organization of precipitation, and alone A_m does not describe important spatial characteristics such as the total area coverage, proximity, location, shape, and gradients of precipitation intensity of precipitation features. A number of other measures of large-scale clustering are analyzed and the interrelationship between a subset of metrics is presented in Figures S1 and S2 of Supporting Information S1. An important aspect of our method is that, by definition, regions of heavy precipitation occupy 5% of the domain on average. Thus, when comparing two climates, the time-mean area covered by heavy precipitation $\overline{C}$ remains constant. Differences in the mean area of features, A_m, between climates are entirely due to a reorganization of precipitation, where an increase in A_m increases the general proximity of heavily precipitating points to each other in that the number of distinct precipitation features (N) is reduced (since N is related to the mean area, A_m, by $A_m = C/N$). However, the above constraint does not apply to the heavy precipitation distribution during a given month. Indeed, as we shall see, an important driver of variations in tropical precipitation clustering in interannual variability is the area coverage of heavy precipitation, C. We therefore consider the behavior of both the mean area of heavy precipitation features, A_m, and the area coverage of heavy precipitation, C, in our analysis below.

2.4. Describing Relationships Between Large-Scale Clustering of Heavy Precipitation and the Mean Climate

Having quantified large-scale precipitation clustering, we seek to characterize the relationships between such clustering and other large-scale climate variables. Specifically, we consider these relationships for interannual variability in both models and observations, and for changes in climate across the CMIP6 ensemble. Throughout, we define interannual variability in a given variable by deseasonalized monthly anomalies, calculated as the monthly mean anomaly from the climatology of the associated month after detrending the time series. The trend is estimated by a first-order linear least squares regression of the data at each location from the daily (precipitation-based metrics) or monthly (all other metrics) time series. However, relationships are consistent regardless of whether the linear trend is removed or not.

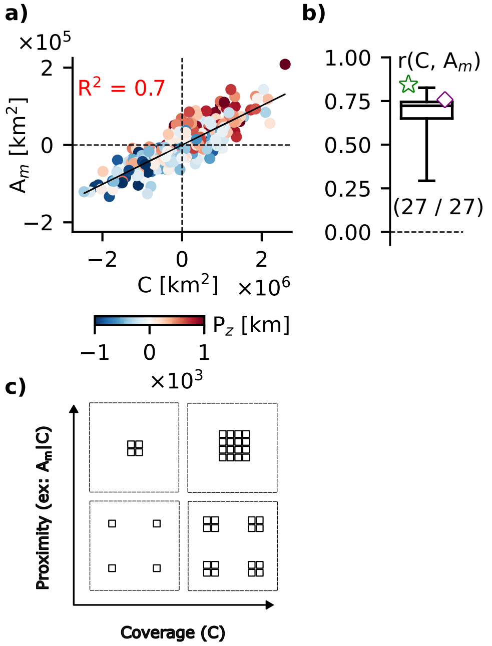

Figure 3. Scatter plot of monthly anomalies in area coverage of heavy precipitation, C, and the mean area of heavy precipitation features, A_m, colored by the zonal proximity of heavy precipitation to the longitude 180°E in the central Pacific, P_z, for GPCP observations (a). Boxplot of the correlations between C and A_m for the CMIP6 ensemble (b). The fraction of CMIP models with statistically significant correlations is indicated below the box, and the GPCP (star) and high-resolution GCM (diamond) correlations are shown in lighter colors if not statistically significant. Schematic of the relationship between the number, N, and mean area of heavy precipitation features, A_m, and coverage of heavy precipitation, C (c). A_m increase from bottom left to top right panel, N decrease from bottom right to top left panel, and a spatial clustering in this framework is interpreted as increasing A_m for a given C, denoted $A_m|C$.

As we will see, for interannual variability, the mean area of features, A_m, and the area coverage of precipitation, C, are strongly correlated with each other and to the large-scale climatic state. Variations in C may be viewed as a temporal clustering of heavy precipitation, since the average of C is 5% of the tropical area by construction. However, this complicates comparisons between interannual variability and climate change; C remains invariant in different climates, and only changes in A_m are relevant. To address this, for interannual variability, we consider the effect of A_m independent of changes in C using the method of partial correlations (Mardia et al., 1979). The partial correlation $r(X,Y|Z)$ represents the relationship between variables X and Y after the removal of the effect of Z, and is given by

$$r(X,Y|Z) = \frac{r(X,Y) - r(X,Z)r(Y,Z)}{\sqrt{1-r^2(X,Z)}\sqrt{1-r^2(Y,Z)}}, \tag{2}$$

where $r(X,Y)$ is the regular correlation between X and Y. A visualisation of the use of partial correlations for this conceptual decomposition is shown in Figure 3a for the observations and Figure 3c for a synthetic idealised rainfall distribution. A_m increases both upwards and to the right, but C only increases horizontally. The vertical direction then describes changes in A_m independent of C. The relationship between changes in clustering along this axis on another climate variable X is estimated as the partial correlation $r(X,A_m|C)$. For partial correlations and simple linear regression, relationships are considered significant if the correlation coefficient is large relative to its uncertainty, as quantified by a standard two-sided t-test, such that the probability of observing a correlation by chance under the null hypothesis of no correlation is below 5%. However, further robustness testing is applied for model-spread correlations, in which potential outliers are removed before calculating the correlation and significance.

3. Spatial Patterns of Heavy Rainfall Clustering

The purpose of this section is to elucidate the spatial patterns of precipitation that produce a high degree of clustering. We first consider how clustering changes in interannual variability before we investigate the spatial patterns associated with increases in clustering with warming across the CMIP6 ensemble.

Figure 2 shows the regression of monthly anomalies in the frequency of occurrence of heavy precipitation, FOO, onto the mean area of heavy precipitation features, A_m, for the observations. When tropical precipitation is observed to be highly clustered on the large scale, heavy precipitation tends to occur more frequently in the central equatorial Pacific. Figure 2 is calculated for all months, but similar spatial patterns can be seen in individual months, strongest in DJF (Figure S3 in Supporting Information S1). Other notable spatial characteristics of the regression include a decrease in heavy precipitation over the Maritime Continent and a small but statistically significant (crosses) decrease in heavy precipitation over the Amazon and Atlantic.

To quantify the shift of heavy precipitation to the central equatorial Pacific, we define the proximity metrics P_z, P_{eq} and P_{heq}, which represent the negative mean distance to the meridian given by the longitude 180°E, the equator, and the hydrological equator respectively (Figure 4 schematic). Here the hydrological equator is defined as the latitude of highest specific humidity at 700 hPa as a function of longitude and time in months. The negative distance was chosen to represent increasing proximity (or clustering) with increasing value and to facilitate the interpretation of the sign of correlations. P_z and P_{eq} use somewhat arbitrary zonal and meridional reference lines with which to describe the zonal and meridional shifts in precipitation, and a more nuanced description may include shifts relative to the climatological distribution. For example, northerly shifts relative to the northern hemisphere climatological convergence zone or southerly shifts relative to the climatological SPCZ or both. However, for simplicity, we use P_z and P_{eq} defined based on 180°E and the equator.

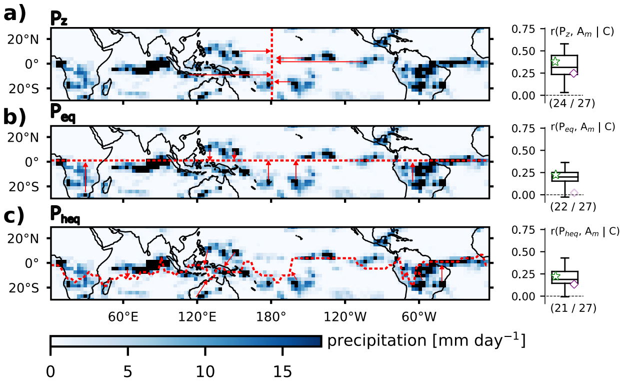

Figure 4. A snapshot of precipitation with reference lines illustrating the calculation of P_z, distance to the meridional red line in (a), P_{eq}, distance to the zonal red line in (b), and P_{heq}, distance to the hydrological equator, red line in (c). The boxplot of the partial correlations with A_m outside the influence of C is shown to the right of each illustration for the observations and GCMs. The fraction of CMIP models with statistically significant correlations is indicated below each box, and the GPCP (star) and high-resolution GCM (diamond) correlations are shown in lighter colors if not statistically significant.

As expected from the regression map, there is a strong relationship between the mean area of features, A_m, and P_z. However, as shown in Figure 3a, there is also a strong observed relationship in interannual variability between A_m and the total area coverage of heavy precipitation, C ($r^2(C, A_m) \sim 0.7$), with greater C favoring greater A_m. This suggests a large part of the observed regression pattern is due to the effect of changes in the total precipitating area, rather than a pure spatial redistribution of a fixed number of heavily precipitating points. This complicates the interpretation of increased clustering in internal variability, since when comparing climates, the mean area coverage of heavy precipitation $\overline{C}$ remains fixed at 5%. To address this, we estimate the variations in the distribution of heavy precipitation that contribute to variations in A_m independent of changes in C using Pearson partial correlation (see Methods).

Observed P_z, P_{eq} and P_{heq} are positively correlated with the mean area of heavy precipitation features, A_m, when the effect of changes in the area coverage of heavy precipitation, C, is removed (star in Figures 4a–4c), suggesting that there is a shift of heavy rainfall toward the equator and the central Pacific when the tropics are highly clustered. For a given C, this contraction of heavily precipitating regions explains about 5%–10% of the remaining variance in A_m after the effect of changes in C is removed.

Both the CMIP ensemble and the high-resolution model generally show similar spatial patterns associated with increasing large-scale clustering (Figure S4 in Supporting Information S1). All models show significant relationships between A_m and C, although on average somewhat weaker than in observations (Figure 3b), and most models (~22/27) show significant positive partial correlations between A_m and the proximity metrics after removing the effect of changes in C (Figures 4a–4c). That is, as for the observations, most models agree that higher clustering, as measured by a larger mean area for a given area coverage of heavy precipitation features, is associated with a shift in heavy precipitation to the central equatorial Pacific. Interestingly, the high-resolution GCM did not show a significant partial correlation with P_{eq}, suggesting clustering in that model is not sensitive to the meridional contraction of heavy precipitation to the geographic equator.

We now consider how large-scale clustering of heavy precipitation changes under climate change. Bläckberg and Singh (2022) noted that large-scale clustering increases as the climate warms in projections of climate change by the CMIP5 ensemble. Figure 5a shows that this is also true for CMIP6; all models project an increase in A_m with warming to varying degrees. However, there is a wide spread in climatological A_m and wide spread in climatological increase in A_m across the ensemble, suggesting the degree of large-scale clustering and the change in large-scale clustering with warming is poorly constrained in the models.

Given the climatologically fixed C in this framework, changes in the mean area of precipitation features, A_m, with warming are driven entirely by a spatial reorganization of convection to larger features. The present analysis evaluates whether the spatial patterns associated with a high degree of clustering of precipitation in interannual variability may also be relevant to the redistribution of heavy precipitation due to the forced response from global warming. Indeed, all but one model show an increase in P_{eq} with warming, indicating a contraction of heavy precipitation towards the geographic equator (Figure 5b) and all models contract heavy precipitation towards the hydrological equator (Figure 5c). One possible interpretation of this is that a narrowing of the ITCZ provides a mechanism for the overall increase in clustering with warming. However, we note that the change in P_{eq} and P_{heq} with warming is uncorrelated with the change in A_m across the CMIP6 ensemble; models exhibiting stronger ITCZ narrowing with warming do not show stronger increases in large-scale clustering of precipitation. On the other hand, there is a significant correlation between increases in mean area of precipitation features, A_m, and changes in P_z across the CMIP6 ensemble. That is, models that show a greater clustering with warming also show a zonally smaller expansion/greater contraction of heavy precipitation from/to the central Pacific (note that the zonal and meridional contractions are somewhat anticorrelated, as also identified by Popp and Bony (2019)).

Going beyond the simple distance metrics, Figure 6 regresses the projected increase in frequency of occurrence of heavy precipitation onto the projected increase in A_m across the CMIP ensemble. This reveals a spatial pattern of precipitation changes with several similarities to the pattern for interannual variability shown in Figure 2. However, an important distinction is that, for changes with warming the total area of heavy precipitation, C, is fixed. Similarities between the regression patterns include a regression coefficient largest in the central Pacific close to the equator, and a redistribution of precipitation away from the Maritime Continent, Amazon, and Atlantic. While in interannual variability heavy precipitation shifts southward in the Pacific for highly clustered states, the changes with warming show a northward shift of heavy precipitation in the Pacific.

We note that the spatial patterns associated with a climatologically high degree of clustering of heavy precipitation across the CMIP6 ensemble (Figure S5 in Supporting Information S1) are rather different from those of internal variability and changes with warming. Models with high climatological values of A_m tend to have more convection in the warm pool, over tropical continents, and at the edges of the northern and southern convergence zones over the Pacific Ocean. These relationships cannot be summarized by a single value of either P_z, P_{eq}, or P_{heq}. Rather, we find that high climatological values of A_m are associated with high month-to-month variability in C. This indicates that high climatological clustering corresponds to high clustering in time, with some days producing a large amount of heavy precipitation across the tropics and other days producing much less.

In summary, the spatial patterns of heavy precipitation associated with highly clustered states vary across timescales, but there are important common threads. In both internal variability and for changes with warming, higher clustering as measured by A_m is associated with more heavy precipitation in the central equatorial Pacific. In particular, models with stronger increases in large-scale clustering of precipitation under warming also exhibit a relatively greater zonal shift in convection to the central Pacific. This potentially suggests the Walker circulation, and the East–West SST gradient in the Pacific, as an important control on the magnitude of changes in large-scale clustering of precipitation with warming. We next investigate the mechanisms associated with large-scale clustering, including SST changes, cloud-radiative feedbacks, and a "narrowing of the ITCZ" in both internal variability and under climate change.

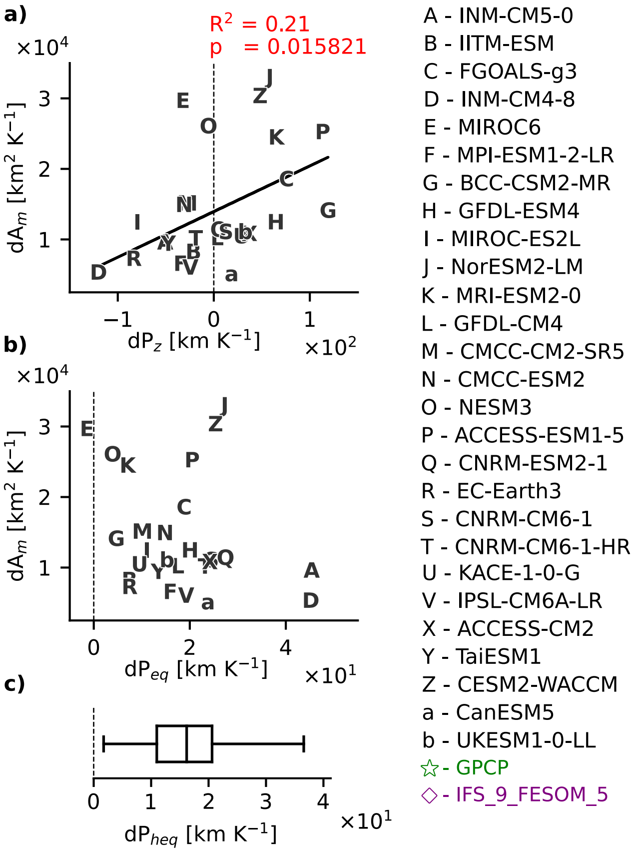

Figure 5. Changes in clustering statistics with warming in the CMIP6 ensemble. Scatter plot of change in climatological mean area of heavy precipitation features, A_m, with change in climatological mean distance of heavy precipitation to the central Pacific, P_z (a), change in mean heavy precipitation proximity to the geograhic equator, P_{eq} (b), and boxplot of change in climatological mean distance to the hydrological equator, P_{heq} (c). The hydrological equator is defined as the latitude of highest specific humidity at 700 hPa as a function of longitude and time in months. All quantities are normalized by the tropical-mean surface temperature change (land and ocean) from the historical to the SSP585 scenario simulation period in each model.

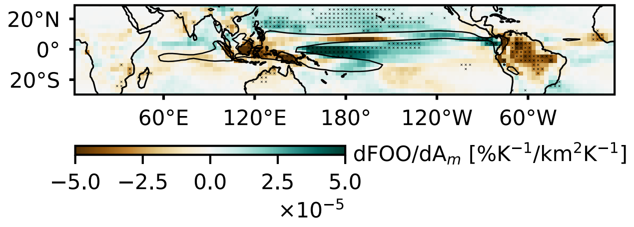

Figure 6. Increase in frequency of occurrence of heavy precipitation, FOO, regressed onto increase in A_m per kelvin tropical-mean surface temperature change from the historical to the SSP585 scenario simulation period across the CMIP6 ensemble. Contour shows the ensemble-mean 90th percentile of FOO in the historical period and crosses indicate whether correlations are statistically significant.

4. Mechanisms Associated With Heavy Rainfall Clustering

This section investigates the extent to which changes in the El Niño-Southern Oscillation (ENSO) can explain changes in clustering, discusses whether top of the atmosphere radiative fluxes may positively feedback on the highly clustered states, and if a meridional clustering of heavy rainfall with warming is related to constraints on the tropical ascent area fraction.

We use the Southern Oscillation Index (SOI; Ropelewski & Jones, 1987) and the Oceanic Niño Index (ONI; Sobel et al., 2002) to identify the state of the El Niño-Southern Oscillation in interannual variability and compare ascent area fraction, A_a, using the area where the 500 hPa vertical pressure velocity is negative. The SOI represents the standardized deseasonalized monthly anomalies of the surface pressure difference between Tahiti (17.6°S, 149.6°W) and Darwin (12.5°S, 130.9°E), calculated here as the 3-month rolling average. The ONI represents the 3-month rolling average SST anomaly in the Niño3.4 region (5°S–5°N, 120°–170°W), calculated here relative to the full range of years used in the climatology. SOI (ONI) values less (greater) than −7 (0.5) represent El Niño conditions and SOI (ONI) values greater (less) than 7 (−0.5)

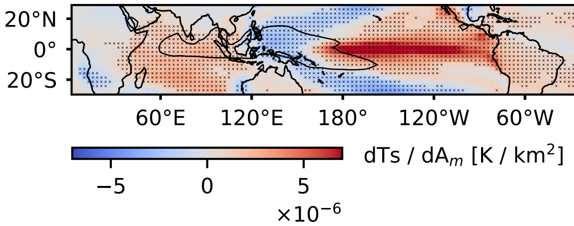

Figure 7. NOAA-GlobalTemp surface temperature (land and ocean), T_s, regressed onto A_m for interannual variability. The contour shows the climatological 90th percentile of T_s, and crosses indicate whether correlations are statistically significant.

represent La Niña conditions. The climatological East–West Pacific SST gradient, defined as the time-mean difference between the SST in the western- (5°S–5°N, 80°–150E) and eastern (5°S–5°N, 180°–80°W) Pacific boxes, which we denote T_z, serves as an indicator for climatologically "El Niño-like" conditions (Watanabe et al., 2024).

Observations show several indications that highly clustered states, corresponding to large values of the mean area of heavy precipitation features, A_m, are associated with El Niño-like conditions in interannual variability. First, surface temperature regressed onto A_m shows a pattern strongly reminiscent of an El Niño SST signature (Alexander et al., 2002) (Figure 7). Second, during times of ONI exceeding 0.5°C compared to all days, A_m increases as heavy precipitation moves from the maritime continent towards the central Pacific (Figure S6 in Supporting Information S1). Finally, in absolute value and independent of changes in C, SOI and ONI show correlations with A_m consistent with heavy precipitation in a more clustered state during El Nino like conditions (Figure 8a and Figure S1 in Supporting Information S1). Examination of snapshots of observed precipitation features during El Niño and La Niña conditions suggest that a greater mean area of heavy rainfall is favoured during El Niño conditions due to a greater total area coverage of heavy precipitation locally growing precipitation features in combination with more frequently forming large connected components (precipitation features) in the central Pacific (Figure 1c). From these results, we may argue ENSO as a driver for interannual variability in clustering, however, it is possible that radiative effects associated with clustering may feedback on its development and maintenance. To investigate this possibility, we regressed the CERES top-of-atmosphere radiative fluxes onto changes in A_m in interannual variability. High A_m is associated with positive clear-sky and cloud radiative forcing in the central Pacific, which could lead to an amplification of the pattern of heavy precipitation frequency associated with high A_m. However, the top-of-atmosphere forcing does not strongly project onto the ONI, and any feedback between clustering and El Niño is therefore likely to be weak (Figure S7 in Supporting Information S1).

Most CMIP models capture the observed connection between SOI and A_m (Figure S1 in Supporting Information S1) and the independent contribution of SOI on A_m outside the influence of C, as does the high-resolution GCM (Figure 8b). Thus, both models and observations show that large-scale clustering of precipitation is greater during El Niño than La Niña in interannual variability. This is despite the fact that El Niño represents a weakening of the Walker circulation and a weakening of tropical SST gradients, both of which are generally thought to facilitate the organization of convection on large scales.

The above result contrasts with those of Quan et al. (2025), who found rainfall clustering to be higher under La Niña-like conditions using idealized SST-pattern forced simulations and a measure of clustering based on the Gini-index of the precipitation distribution. When the same Gini index-based measure is applied to interannual variability, however, we find more clustered states under El Niño, indicating that the discrepancy arises as a result of the particular forcing used. Nevertheless, the conclusion that clustering is favoured under El Niño conditions may be sensitive to how clustering is defined, for example, whether increased area coverage, C, is considered more or less clustered, and the spatial resolution of the precipitation data set.

The strong connection between El Niño conditions and clustering in interannual variability motivates the investigation of changes in the climatological Pacific SST gradient to a more El Niño-like state as a mechanism for explaining model-spread in projected changes in clustering. Consistent with expectations, the magnitude of the weakening of the East–West Pacific SST gradient explains a similar amount of variance in projected changes in clustering as the zonal shift in heavy precipitation (Figure 9). Models that have more El Niño-like warming patterns tend to exhibit larger increases in large-scale clustering of precipitation. Regressing the SST changes against projected changes in the mean area of precipitation features, A_m, also shows an El-Niño-like pattern, with a relative warming in the east and relative cooling

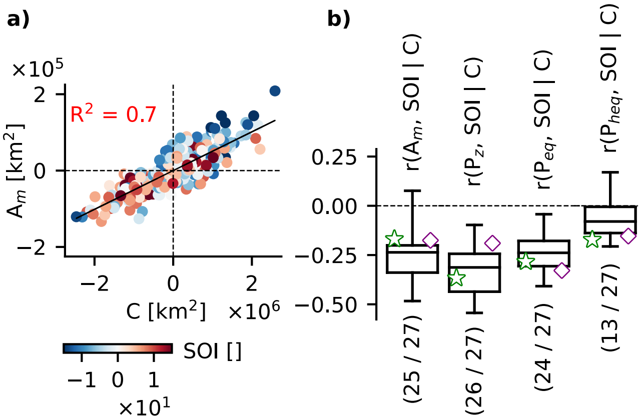

Figure 8. Same as Figure 3, but with the Southern Oscillantion Index (SOI) in scatter colors and as explanatory variable in boxplot.

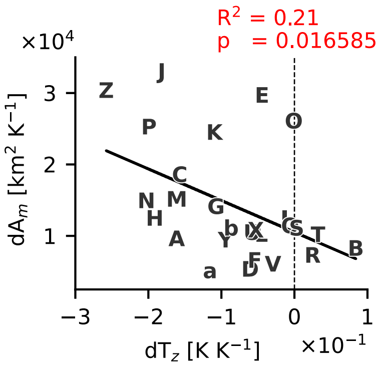

Figure 9. Same as Figure 5a, but with the change in the climatological Pacific SST gradient, T_z, per kelvin tropical-mean surface temperature change from the historical to the SSP585 scenario simulation period across the CMIP6 ensemble as explanatory variable. Models are as given in the legend in Figure 5.

in the west (Figure 10). In addition, the regression pattern has a noticeable north-south gradient, consistent with the positive regression coefficients for heavy precipitation frequency north of the equator in Figure 6.

Note, while changes to the Pacific SST gradient may be climatologically argued as a driver for changes in clustering with warming there are changes in the zonal SST gradient, T_z, and the mean distance of heavy precipitation to the central Pacific of both signs across the 27 CMIP6 models we analyse, suggesting that zonal shifts in convection are not the primary reason for the ensemble-mean increase in large-scale clustering with warming that we document. We hypothesize that the ensemble-mean increase in A_m is instead associated with a meridional shift in convection. All but one model increases proximity of heavy precipitation to the geographic and hydrological equator with warming, and this is associated with an increase in the large-scale clustering of precipitation in natural variability. The increased proximity of heavy precipitation to the hydrological equator with warming can be interpreted as a meridional clustering of convection to the centre of the ITCZ, or a “narrowing” of the ITCZ.

Mechanistically, changes to the “width” or area of the ITCZ characterized by changes in the tropical ascent area fraction relative to descent area fraction are theorized to be controlled by convective limitations on the efficiency of moisture and heat export from the ITCZ to its surroundings (the Gross Moist Stability) (Byrne & Schneider, 2016). From this framework, the forced response to global warming modulate the “width” (or area) of the ITCZ to maintain the energy balance between regions of ascent and descent. Here, we find a relatively strong relationship between the ascent area fraction, A_a, and the proximity of heavy rainfall to the hydrological equator, P_{eq}, with models in which A_a decreases with warming tending to also exhibit larger increases in P_{heq} (Figure 11). This suggests that the mechanisms for ITCZ narrowing described by Byrne and Schneider (2016) are also relevant when one is considering large-scale clustering of precipitation.

In this section we have shown that El Niño-like states tend to result in a higher degree of clustering in both interannual variability and across the CMIP6 ensemble under climate change. Further, we have highlighted that cloud-radiative feedbacks and energetic constraints on the large-scale circulation of moisture and heat (Byrne & Schneider, 2016) may influence the manifestation of clustering in interannual variability and for climatological changes with warming, respectively. In the next section, we explore the relationship between large-scale clustering and the tropical humidity and cloud distributions, and whether this has any implications for climate sensitivity.

5. Heavy Rainfall Clustering and Radiative Feedbacks Associated With Climate Sensitivity

We now consider how large-scale clustering of precipitation connects to the cloud and humidity distributions. Our motivation is to understand how such clustering may influence radiative feedbacks. Previous authors have found that the degree of clustering on different spatial scales is linked to the radiation budget and clouds (e.g., Bony et al., 2020; Pendergrass et al., 2016; Wing & Emanuel, 2014). The literature suggests changes in clustering under warming may be associated with cloud feedbacks and in extension equilibrium climate sensitivity (ECS) (Schiro et al., 2022). This section investigates this hypothesis for large-scale clustering across the CMIP6 ensemble. As for previous sections, the analysis assesses whether relationships in interannual variability can be used to infer the response to climate change, raising the possibility of an observational constraint on particular radiative feedbacks or ECS itself.

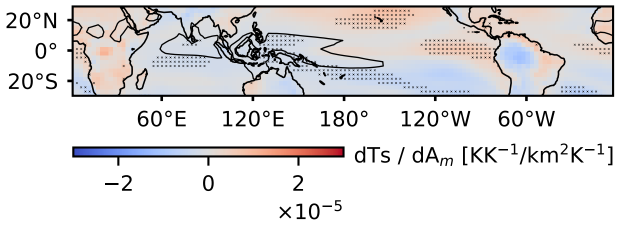

Figure 10. Change in surface temperature, T_s, regressed onto change in mean area of heavy precipitation features, A_m, per kelvin tropical-mean surface temperature change from the historical to the SSP585 scenario simulation period across the CMIP6 ensemble. Contour shows ensemble-mean 90th percentile climatological T_s and crosses indicate if correlations are statistically significant.

Rather than focusing on changes in radiative fluxes or calculating feedback strength directly, we focus on changes in mid-tropospheric relative humidity, which has been argued to cause a negative longwave feedback associated with changes in convective organization (Bony et al., 2020; Tobin et al., 2013), and

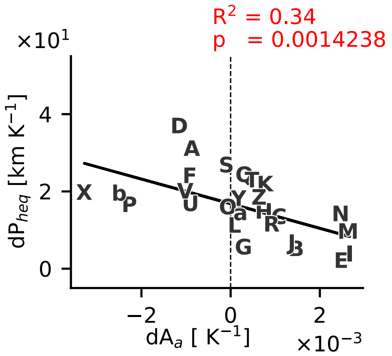

Figure 11. Same as Figure 5a, but with the change in climatological area of ascent, A_a, per kelvin tropical-mean surface temperature change from the historical to the SSP585 scenario simulation period across the CMIP6 ensemble as explanatory variable. Here, the climatological area of ascent is calculated as the climatological time-mean of the fraction of the tropical domain where the monthly mean 500 hpa vertical pressure velocity is negative. Models are as given in the legend in Figure 5.

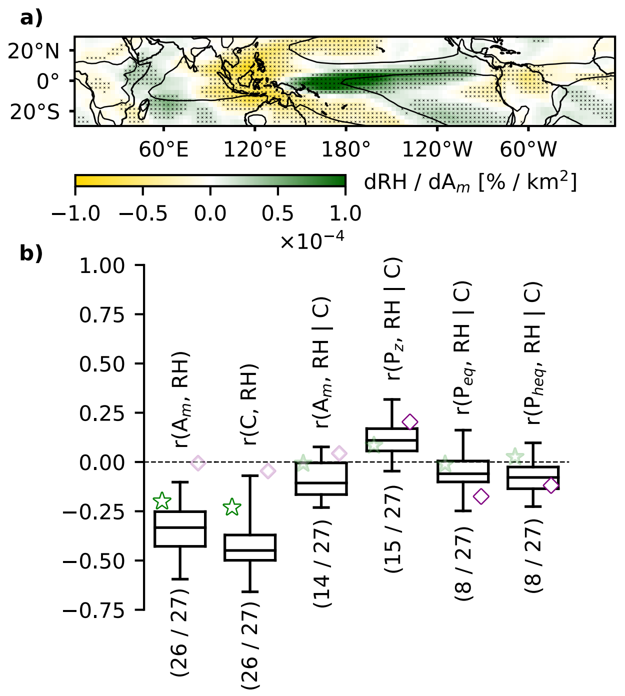

Figure 12. Relative humidity at 500 hPa, RH, regressed onto mean area of heavy precipitation features, A_m, in interannual variability (a). Boxplots of correlations and partial correlations outside the influence of the total area coverage of heavy precipitation, C, between RH and A_m, proximity of heavy precipitation to 180°E, P_z, and proximity of heavy precipitation to the geographic-, P_{eq}, and hydrological equator, P_{heq} (b). The star and diamond show results for observations and the high-resolution GCM, respectively, shown in lighter colors if not statistically significant. The numbers below the boxplots give the fraction of models with statistically significant correlations.

changes in low-cloud fraction in regions of subsidence, which have been argued to cause a positive shortwave feedback associated with changes in convective organization (Schiro et al., 2022). Changes in low clouds in regions of subsidence are also known to be important for understanding model spread in ECS (Zelinka et al., 2020). Correlations between measures of large-scale clustering of heavy precipitation and various other metrics commonly used to assess changes to the radiation budget on interannual and climatological timescales are presented in Figures S1 and S2 of Supporting Information S1.

For our analysis, the mid-tropospheric relative humidity, RH, is taken as the 500 hPa value. Observed low-cloud fraction, LCF, is calculated using the ISCCP weather states (Tselioudis et al., 2010) as described in Section 2.2, and taken as the cloud fraction below 600 hPa. CMIP6 low-cloud fraction is calculated analogously, with cloud fraction pre-processed by interpolating hybrid-sigma coordinates to 19 pressure levels if not already available on pressure levels. We also consider the mean low-cloud fraction in regions of descent, denoted by a subscript d and calculated as the tropical-mean of gridpoints for which the monthly mean vertical pressure velocity at 500 hPa is positive. Later we will consider variables in regions of ascent, defined analogously for negative 500 hPa vertical pressure velocity and identified by a subscript a.

Figures 12a and 13a show observational estimates of the regression patterns of RH and LCF against the mean area of precipitation features, A_m, for interannual variability. The regressions show a clear El-Niño-like pattern, with increases in RH and decreases in LCF in the central and eastern Pacific, and opposite changes over the warm pool (Figure S8 in Supporting Information S1). This suggests the changes in RH and low clouds with increased tropical clustering are caused at least in part by variations associated with El Niño-Southern Oscillation.

From a tropics-wide perspective, when the observed degree of clustering is high according to A_m, the tropical mean is drier (Figure 12b) while LCF increases, both when averaged over descending grid points (LCF$_d$ in Figure 13b) and in regions of time-mean descent (contour on Figure 13a). The environmental signature associated with large-scale clustering is therefore consistent with a negative longwave feedback identified for large-scale clustering in idealized simulations (Arnold & Randall, 2015) and a longwave- and low-cloud cooling signature found associated with interannual variations in mesoscale organization in observations (Bony et al., 2020). Partial correlations of A_m with RH excluding the influence of the total area coverage of heavy precipitation, C, are insignificant in the observations (Figure 12b). This suggests that the influence of A_m on relative humidity is almost entirely due to increasing C. We note that this correlation exhibits some sensitivity to the percentile threshold used to define heavy precipitation, and shows a statistically significant negative correlation when using the 90th percentile ($r \sim 0.25$). Observed correlations of relative humidity and the distance metrics P_{eq}, P_{heq} and P_z, representing proximity of heavy rainfall to the equator and the central Pacific, respectively, are also insignificant. Observed LCF$_d$ on the other hand increases for all three forms of spatial clustering, outside the influence of C (Figure 13b).

The CMIP6 ensemble generally agrees on the strong association between C and the aforementioned tropical environmental signatures. However, unlike the observational estimates, about half of the models also show a significant relationship between relative humidity and spatial shifts of heavy

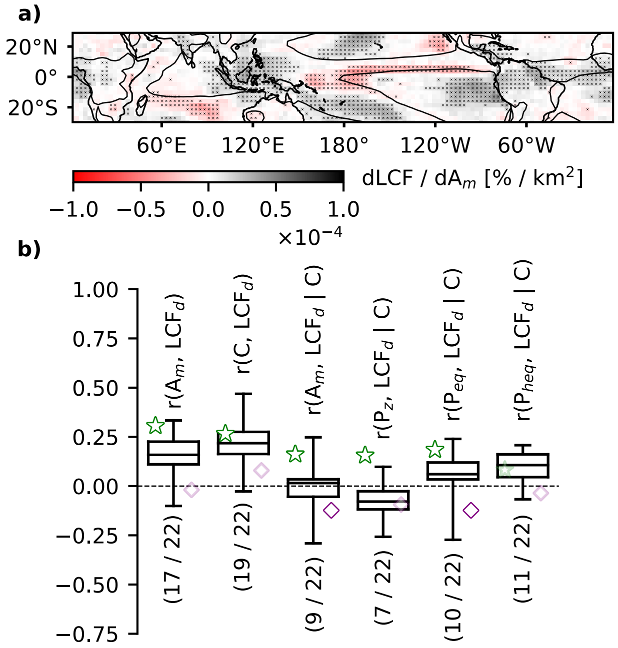

Figure 13. Same as Figure 12, but with the low cloud fraction, LCF, and low cloud fraction in regions of descent, LCF$_d$, as response variable.

precipitation (Figure 12b). In particular, in a subset of models, zonal shifts in heavy precipitation to the central Pacific are (independent of variations in C) associated with a moistening in the tropics, while meridional shifts to the equator are associated with a domain-mean drying. These relationships are also present in the high-resolution GCM. The models generally do not capture the observed LCF$_d$ signature for clustering outside the influence of C, except for a subset of CMIP models producing increases in LCF$_d$ for meridional shifts in heavy precipitation (Figure 13b). Other notable independent effects of the spatial preference of heavy precipitation on environmental conditions include a reduction in high cloud fraction above 400 hPa in regions of ascent, HCF$_a$, with observed and modelled meridional shifts in precipitation ($r\left(P_{eq}, HCF_a | A_f\right) \sim 0.25$).

Our analysis of interannual variability has revealed moderate relationships between tropical-mean RH and low-cloud fraction and large-scale clustering of precipitation in observations. However, in observations, the RH relationships are primarily driven by changes in the total area coverage of heavy precipitation, C. C also influences low cloud fraction, LCF$_d$, but spatial shifts in heavy precipitation retains a connection to LCF$_d$ outside the influence of C in observations. We now consider relationships between RH and low-cloud fraction changes and changes in the clustering of precipitation in climate projections.

Consistent with the results from the previous section, models with larger increases in large-scale clustering under warming tend to have changes in relative humidity and clouds indicative of an El Niño-like shift in the tropical circulation. The regression patterns of RH and LCF onto changes in A_m under warming across the CMIP6 ensemble are similar to those for interannual variability presented above (Figures S10a and S10b in Supporting Information S1). In both interannual variability and for changes with warming, the frequency of low clouds increases in the southeast Pacific subsidence region, where EIS is thought to be the dominant control on the low cloudiness (Scott et al., 2020; Wood & Bretherton, 2006) (Figure S9 in Supporting Information S1). However, in contrast to the case for interannual variability, changes in clustering according to A_m with warming have little connection to changes in tropical-mean RH or low-cloud fraction in regions of descent, LCF$_d$, across the CMIP6 ensemble (Figures 14a and 14b and Figure S2 in Supporting Information S1). Given this, it is perhaps not surprising that there is no correlation between the increase in A_m within a model under warming and the model's ECS (Figure 14c). Here we take ECS from the supplementary material of Zelinka et al. (2020) and Hausfather et al. (2022).

The results therefore indicate that a general clustering of heavy precipitation, according to A_m, under warming does not provide a robust explanation for changes in radiative feedbacks, despite indications from observations that more clustered states in this way are drier with more low-clouds in regions of large-scale descent. One reason for this result appears to be the different ways in which large-scale clustering of heavy rainfall can manifest at different timescales. In interannual variability, increases in heavy precipitation clustering are associated with increases in the total area coverage of heavy precipitation, defined here by C. Under climate change, increases in C in 1 month must be balanced by decreases in another month such that the overall average must remain constant. When the effects of changes in total area coverage are removed, the observed relationship to RH becomes weak. However, this explanation is not the whole story, as many of the models do exhibit changes in RH associated with increased clustering independent of changes in the total area coverage of heavy precipitation. Even among this subset of models, however, the future increase in A_m is not a good predictor of future changes in clouds or relative humidity. This suggests that caution should be used in extrapolating relationships—either observed or simulated—between large-scale clustering and other properties of the climate in internal variability to those for climate change.

Finally, we note that there does exist a relationship between a tropical-mean drying and LCF in some key subsidence regions with the proximity of heavy rainfall to the geographic and hydrological equator (Figures S10e–S10h in Supporting Information S1). Under warming, variations in the meridional contraction of heavy rainfall, as measured by the mean distance of heavily precipitating gridpoints to the equator P_{eq}, explain about

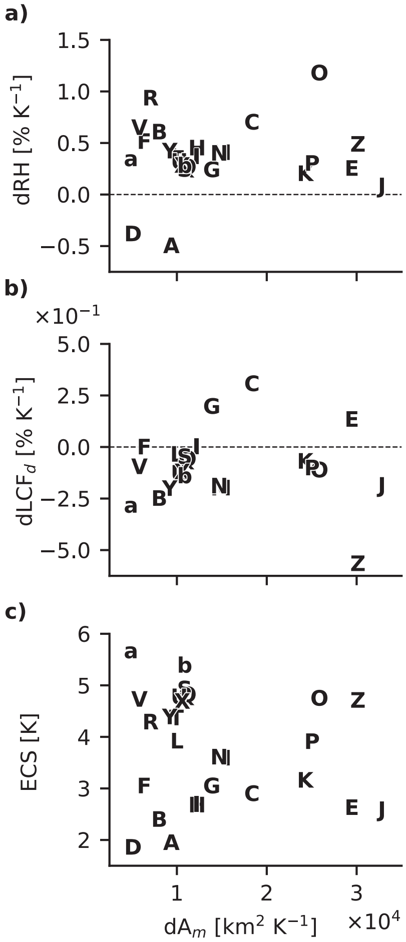

Figure 14. Scatter plot of change in A_m between historical period and SSP585 period per kelvin tropical-mean surface temperature change and associated tropical-mean change in 500 hPa relative humidity, RH, (a), low cloud fraction in regions of descent, LCF$_d$ (b), and equilibrium climate sensitivity (ECS) in the CMIP6 ensemble (c). Models are as given in the legend in Figure 5.

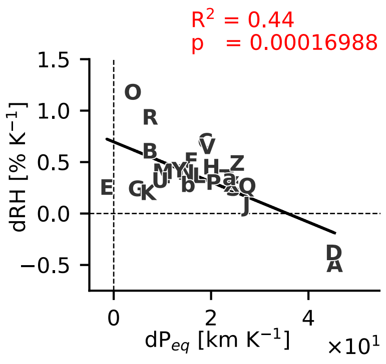

Figure 15. Scatter plot of change in mean distance of heavy precipitation to the geographic equator, P_{eq}, between historical period and SSP585 period per kelvin tropical-mean surface temperature change and associated tropical-mean change in 500 hPa relative humidity, RH. Models are as given in the legend in Figure 5.

45% of the variance in tropical-mean drying (Figures 15 and 16). This relationship is consistent with the sign of the relationship between RH and P_{eq} in interannual variability in a subset of CMIP6 models (Figure 12b). This result potentially highlights the importance of ITCZ narrowing as a specific manifestation of large-scale clustering that appears to be important for setting the tropical-mean relative humidity. However, we note that most of the spread in projected drying is due to the result of four models with dramatically different drying trends. When these 4 models are removed from the ensemble, the correlation is no longer present. Thus, further work is required to confirm if this relationship is robust and physical.

6. Summary and Discussion

In this paper we have (a) presented the dominant spatial patterns of heavy precipitation that produce a high degree of clustering on the large scale (Section 3); (b) tied the associated spatial patterns to mechanisms associated with clustering through large-scale SST patterns (Section 4); and (c) evaluated the associated changes in properties of the atmosphere that are important for the radiation budget (Section 5) in both interannual variability and for projected changes with warming. We have defined the degree of clustering of precipitation based on the spatial distribution of the top 5% heaviest daily rainfall instances, with high general clustering corresponding to scenes in which the mean area of individual precipitation features is large. A challenge in any definition of convective organization is in how one measures organization consistently as the total amount of precipitation changes (Retsch et al., 2020; Tobin et al., 2013). In the present study, the use of a percentile precipitation threshold accounts for changing mean precipitation rates in different climates. However, in internal variability, the mean area of precipitation features is affected by both spatial shifts in the precipitation distribution and variations in the total area coverage of heavy precipitation, *C*. This is addressed here by using Pearson partial correlations to evaluate the independent contributions of different measures of the spatial distribution of precipitation while controlling for the effect of *C*.

When tropical precipitation is observed to be highly clustered on the large scale in interannual variability, heavy precipitation gravitates meridionally to the equator and zonally towards the central Pacific. In climate projections, large-scale clustering of precipitation is found to increase in all models, and this coincides with a shift of precipitation toward the equator, across the ensemble. We therefore hypothesize that a narrowing of the ITCZ, negatively correlated with climatological area of ascent, A_a, ($r = -0.58$) may be an important contributor to increases in large-scale clustering of precipitation under warming. This implicates mechanisms related to the limitations of the transport of energy by the Hadley circulation that have been argued to control changes in ITCZ width as a forced response to global warming (Byrne & Schneider, 2016).

On the other hand, the intermodel spread in changes in clustering with warming across the CMIP6 ensemble is related to zonal rather than meridional shifts in the precipitation. This motivated an investigation of the role played by Pacific SST gradients in changes in large-scale clustering of precipitation. In interannual variability, El Niño-Southern Oscillation linked variability appears to be a major driver of variability in large-scale clustering of precipitation, with precipitation during El Niño events more clustered than during La Niña events.

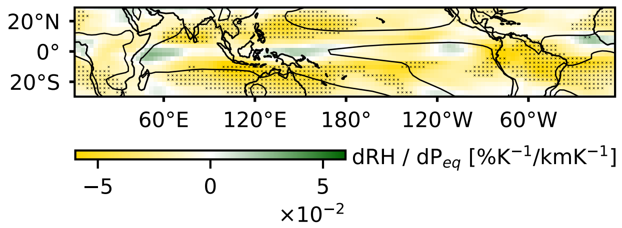

Figure 16. Change in relative humidity at 500 hPa, RH, regressed onto changes in mean distance of heavy precipitation to the geographic equator, P_{eq}, between the historical and SSP585 periods per kelvin warming.

Under warming, changes in zonal SST gradients appeared to explain the sensitivity of projected clustering to zonal shifts in heavy rainfall; those models with more El Niño-like warming patterns tended to exhibit stronger increases in precipitation clustering. This is important given the large disagreement between observed and simulated SST trends in the tropical Pacific (e.g., Wills et al., 2022). Observations show a strengthening of the SST gradient, suggesting a weaker increase in large-scale clustering compared to simulations, which tend to show a weakening of tropical SST gradients.

Finally, we assessed whether changes in a general clustering of heavy precipitation can be used to constrain climate sensitivity. In observed interannual variability, a greater area coverage of heavy precipitation, C, is associated with a drier domain-mean and an increase in low-cloudiness in subsidence regions, LCF$_d$. The connection between clustering for a given C persists for LCF$_d$, but changes in the mean area of precipitation features and meridional and zonal shifts in heavy precipitation generally have weak relationships to the tropical-mean relative humidity, RH, independent of their relationship to C.

GCMs from the CMIP ensemble generally capture the observed tropical environment signatures associated with changes in C, but often have different RH and LCF$_d$ connections to shifts in heavy precipitation independent of C. In contrast to observations, RH in several models is sensitive to both meridional and zonal shifts in heavy precipitation. In CMIP6 models, zonal shifts of precipitation to the central Pacific are associated with a more moist environment, whereas meridional shifts to the equator are associated with a drier environment. Realistically represented or not, these sensitivities appear to affect how these models project relative humidity into the future; the subset of models sensitive to drying from meridional contraction of heavy precipitation create considerable spread in the model ensemble relative humidity changes under warming ($r = -0.66$).

The study includes several limitations that are worth highlighting. Perhaps most importantly, the models we examined do not resolve the processes leading to organization of convection on mesoscales, which in turn may affect how they simulate heavy precipitation associated with large-scale convective features (Bao et al., 2017). This includes the high-resolution GCM, which still employs a parameterized convection scheme (Koldunov et al., 2023). Another limitation is the specific control applied as an energetic constraint across climates and confounding variable for interannual variability. Here we have used the total area covered by the 95th percentile threshold to represent heavy precipitation, which is largely set by the tropical-mean rainfall rate. However, between data sets, climates, seasons, and regions these precipitation thresholds may yield differences in the convective features represented and therefore mechanisms that change its heavy rainfall and associated environment. Finally, we note that our model ensemble is one of opportunity, and the models and temporal- and spatial resolution of variables used were dictated by the available data. Correlation across the ensemble is not guaranteed to be produced by a physical relationship, and the extent to which such relationships arise by chance rise the more variables are examined. Nevertheless, the relationships between SST gradients and shifts in the precipitation distribution we highlight here are based on well-established physical relationships that provide some confidence in their robustness.

Future research is encouraged to adopt the isolation of total area coverage of convection, or other similar controls for changes in the mean precipitation rate, as used in the present framework. One avenue for further investigation is to identify models with realistic clustering compared to observations. The CMIP6 models considered here show a wide range in climatological clustering and internal variability in clustering, and perhaps a subset of models with more realistic clustering characteristics should be given more weight in projections of climate. In a similar way, investigating the connection between large-scale clustering and mesoscale clustering in high-resolution observations and storm-resolving models may further constrain the model spread in projections by identifying unrealistic behavior. Further developing these research endeavors allow for increased confidence and reduce the model uncertainty in aspects of projections that could be influenced by changes in convective organization, ultimately allowing for improvement in mitigation and adaptation strategies for a warming climate.

Conflict of Interest

The authors declare no conflicts of interest relevant to this study.

Availability Statement

CMIP models used in this study are listed in Table S1 of Supporting Information S1 and model output is available through the Earth System Grid Federation (2024). Observational data sets and access are listed here; daily precipitation estimates from the Global Precipitation Climatology Project (2023), ERA5 reanalysis from the Copernicus Climate Data Store (2023), NOAA surface temperature from the NOAA Physical Sciences Laboratory (2023), CERES top-of-atmosphere radiation from the NASA Langley Atmospheric Science Data Center (2023), ISCCP cloud states from the International Satellite Cloud Climatology Project (2023). The IFS_9_FESOM_5 model data is available via the DKRZ World Data Center for Climate (2023). Code examples for reproducing key metric calculations and figures are available at Blackberg (2025a). Key metrics are available at Blackberg (2025b).

Acknowledgments
We acknowledge the World Climate Research Programme's Working Group on Coupled Modelling, which is responsible for CMIP, and we thank the climate modeling groups (listed in Table S1 of Supporting Information S1) for producing and making available their model output. We acknowledge support from the Australian Research Council (ARC) (Grant DP230102077), the ARC Centre of Excellence for the Weather of the 21st Century (Grant CE170100023), and computational resources and services from the National Computational Infrastructure, all funded by the Australian Government. Further, we acknowledge the Deutsches Klimarechenzentrum (DKRZ) for providing resources for using the Levante supercomputer, which facilitated the analysis of the nextGEMS Cycle 2 simulation: IFS_9_FESOM_5 used in this study. We also extend a special thank you to Dr. Cathy Hohenegger at Max Planck Insntitute for Meteorology for hosting the first author during a research visit to Hamburg, for providing guidance on model selection, and for facilitating access to institutional resources that greatly supported the analysis of the high-resolution GCM used in this study. Finally, we thank the two anonymous reviewers for their constructive and helpful comments, which improved the clarity and quality of this manuscript. Open access publishing facilitated by Monash University, as part of the Wiley - Monash University agreement via the Council of Australasian University Librarians.

References

Alexander, M. A., Bladé, I., Newman, M., Lanzante, J. R., Lau, N.-C., & Scott, J. D. (2002). The atmospheric bridge: The influence of ENSO teleconnections on air–sea interaction over the global oceans. *Journal of Climate*, *15*(16), 2205–2231. https://doi.org/10.1175/1520-0442(2002)015⟨2205:TABTIO⟩2.0.CO;2

Arnold, N. P., & Randall, D. A. (2015). Global-scale convective aggregation: Implications for the Madden-Julian oscillation. *Journal of Advances in Modeling Earth Systems*, *7*(4), 1499–1518. https://doi.org/10.1002/2015MS000498

Bao, J., Sherwood, S. C., Colin, M., & Dixit, V. (2017). The robust relationship between extreme precipitation and convective organization in idealized numerical modeling simulations. *Journal of Advances in Modeling Earth Systems*, *9*(6), 2291–2303. https://doi.org/10.1002/2017MS001125

Blackberg, P. (2025). Large-scale clustering of tropical precipitation: Code repository [Software]. *Zenodo*. https://doi.org/10.5281/zenodo.17070290

Blackberg, P. (2025). Metrics for large-scale clustering of tropical precipitation [Dataset]. *Zenodo*. https://doi.org/10.5281/zenodo.16946243

Bläckberg, C. P., & Singh, M. S. (2022). Increased large-scale convective aggregation in CMIP5 projections: Implications for tropical precipitation extremes. *Geophysical Research Letters*, *49*(9), e2021GL097295. https://doi.org/10.1029/2021GL097295

Bony, S., Semie, A., Kramer, R. J., Soden, B., Tompkins, A. M., & Emanuel, K. A. (2020). Observed modulation of the tropical radiation budget by deep convective organization and lower-tropospheric stability. *AGU Advances*, *1*(3), e2019AV000155. https://doi.org/10.1029/2019AV000155

Bretherton, C. S., Blossey, P. N., & Khairoutdinov, M. (2005). An energy-balance analysis of deep convective self-aggregation above uniform SST. *Journal of the Atmospheric Sciences*, *62*(12), 4273–4292. https://doi.org/10.1175/jas3614.1

Byrne, M. P., & Schneider, T. (2016). Energetic constraints on the width of the intertropical convergence zone. *Journal of Climate*, *29*(13), 4709–4721. https://doi.org/10.1175/JCLI-D-15-0767.1

Copernicus Climate Data Store. (2023). Era5 reanalysis dataset [Dataset]. https://doi.org/10.24381/cds.adbb2d47

Doelling, D. R., et al. (2013). Ceres syn1deg-day terra-aqua Modis edition 4a. *NASA Langley Atmospheric Science Data Center DAAC*. https://doi.org/10.5067/CERES/SYN1deg-Day_Terra-Aqua_Edition4A

Earth System Grid Federation. (2024). CMIP6 model output [Dataset]. Retrieved from https://esgf-node.llnl.gov/search/cmip6/

Emanuel, K., Wing, A. A., & Vincent, E. M. (2014). Radiative-convective instability. *Journal of Advances in Modeling Earth Systems*, *6*(1), 75–90. https://doi.org/10.1002/2013ms000270

Eyring, V., Bony, S., Meehl, G. A., Senior, C. A., Stevens, B., Stouffer, R. J., & Taylor, K. E. (2016). Overview of the coupled model intercomparison project phase 6 (CMIP6) experimental design and organization. *Geoscientific Model Development*, *9*(5), 1937–1958. https://doi.org/10.5194/gmd-9-1937-2016

Global Precipitation Climatology Project. (2023). GPCP precipitation dataset [Dataset]. https://doi.org/10.5065/ZGJD-9B02

Hartmann, D. L., Hendon, H. H., & Houze, R. A. (1984). Some implications of the mesoscale circulations in tropical cloud clusters for large-scale dynamics and climate. *Journal of the Atmospheric Sciences*, *41*, 113–121. https://doi.org/10.1175/1520-0469(1984)041⟨0113:SIOTMC⟩2.0.CO;2

Hausfather, Z., Marvel, K., Schmidt, G. A., Nielsen-Gammon, J. W., & Zelinka, M. (2022). Climate simulations: Recognize the "hot model" problem. *Nature*, *605*(7908), 26–29. https://doi.org/10.1038/d41586-022-01192-2

Hersbach, H., Bell, B., Berrisford, P., Horányi, A., Muñoz-Sabater, J., Nicolas, J., et al. (2023). Era5 hourly data on pressure levels from 1940 to present. *Copernicus Climate Change Service (C3S) Climate Data Store*. https://doi.org/10.24381/cds.bd0915c6

Holloway, C. E., Wing, A. A., Bony, S., Muller, C., Masunaga, H., L'Ecuyer, T. S., et al. (2017). Observing convective aggregation. *Surveys in Geophysics*, *38*(6), 1199–1236. https://doi.org/10.1007/s10712-017-9419-1

Huang, B., Yin, X., Menne, M. J., Vose, R. S., & Zhang, H.-M. (2024). NOAA global surface temperature dataset (Noaaglobaltemp), version 6.0. *NOAA National Centers for Environmental Information*. https://doi.org/10.25921/rzxg-p717

Huffman, G. J., Adler, R. F., Behrangi, A., Bolvin, D. T., Nelkin, E. J., Gu, G., & Ehsani, M. R. (2023). The new version 3.2 global precipitation climatology project (GPCP) monthly and daily precipitation products. *American Meteorological Society*, *36*(21), 7635–7655. https://doi.org/10.1175/JCLI-D-23-0123.1

International Satellite Cloud Climatology Project. (2023). ISCCP cloud states dataset [Dataset]. Retrieved from https://isccp.giss.nasa.gov/analysis/climanal5.html

Jones, P. W. (1999). First- and second-order conservative remapping schemes for grids in spherical coordinates. *Monthly Weather Review*, *127*(9), 2204–2210. https://doi.org/10.1175/1520-0493(1999)127⟨2204:FASOCR⟩2.0.CO;2

Koldunov, N., Kölling, T., Pedruzo-Bagazgoitia, X., Rackow, T., Redler, R., Sidorenko, D., et al. (2023). nextgems: Output of the model development cycle 3 simulations for icon and ifs. *World Data Center for Climate (WDCC) at DKRZ*. https://doi.org/10.26050/WDCC/nextGEMS_cyc3

Maddox, R. A. (1980). Meoscale convective complexes. *Bulletin of the American Meteorological Society*, *61*(11), 1374–1387. https://doi.org/10.1175/1520-0477(1980)061⟨1374:mcc⟩2.0.co;2

Mapes, B. E. (1993). Gregarious tropical convection. *Journal of the Atmospheric Sciences*, *50*(13), 2026–2037. https://doi.org/10.1175/1520-0469(1993)050⟨2026:gtc⟩2.0.co;2

Mapes, B. E., & Houze, R. A. (1993). Cloud clusters and superclusters over the oceanic warm pool. *Monthly Weather Review*, *121*(5), 1398–1416. https://doi.org/10.1175/1520-0493(1993)121⟨1398:ccasot⟩2.0.co;2

Mardia, K. V., Kent, J. T., & Bibby, J. M. (1979). *Multivariate analysis*. Academic Press.

NASA Langley Atmospheric Science Data Center. (2023). Ceres syn1deg-day terra-aqua Modis edition 4a [Dataset]. Retrieved from https://asdc.larc.nasa.gov/data/CERES/SYN1deg-Day/Terra-Aqua-MODIS_Edition4A/

NOAA Physical Sciences Laboratory. (2023). NOAA gridded surface temperature dataset [Dataset]. Retrieved from https://psl.noaa.gov/data/gridded/

Pendergrass, A. G., Reed, K. A., & Medeiros, B. (2016). The link between extreme precipitation and convective organization in a warming climate: Global radiative-convective equilibrium simulations. *Geophysical Research Letters*, *43*(21), 11445–11452. https://doi.org/10.1002/2016GL071285

Popp, M., & Bony, S. (2019). Stronger zonal convective clustering associated with a wider tropical rain belt. *Nature Communications*, *10*(1), 4261. https://doi.org/10.1038/s41467-019-12167-9

Quan, H., Zhang, B., Wang, C., & Fueglistaler, S. (2025). The sea surface temperature pattern effect on outgoing longwave radiation: The role of large-scale convective aggregation. *Geophysical Research Letters*, *52*(11), e2024GL112756. https://doi.org/10.1029/2024GL112756

Retsch, M. H., Jakob, C., & Singh, M. S. (2020). Assessing convective organization in tropical radar observations. *Journal of Geophysical Research: Atmospheres*, *125*(7), e2019JD031801. https://doi.org/10.1029/2019JD031801

Ropelewski, C., & Jones, P. (1987). An extension of the Tahiti–Darwin southern oscillation index. *Monthly Weather Review*, *115*(9), 2161–2165. https://doi.org/10.1175/1520-0493(1987)115<2161:aeotts>2.0.co;2

Schiro, K., Su, H., Ahmed, F., Dai, N., Singer, C., Gentine, P., et al. (2022). Model spread in tropical low cloud feedback tied to overturning circulation response to warming. *Nature Communications*, *13*(1), 7119. https://doi.org/10.1038/s41467-022-34787-4

Scott, R. C., Myers, T. A., Norris, J. R., Zelinka, M. D., Klein, S. A., Sun, M., & Doelling, D. R. (2020). Observed sensitivity of low-cloud radiative effects to meteorological perturbations over the global oceans. *Journal of Climate*, *33*(18), 7717–7734. https://doi.org/10.1175/JCLI-D-19-1028.1

Semie, A. G., & Bony, S. (2020). Relationship between precipitation extremes and convective organization inferred from satellite observations. *Geophysical Research Letters*, *47*(9), e2019GL086927. https://doi.org/10.1029/2019GL086927

Sobel, A. H., Held, I. M., & Bretherton, C. S. (2002). The Enso signal in tropical tropospheric temperature. *Journal of Climate*, *15*(18), 2702–2706. https://doi.org/10.1175/1520-0442(2002)015⟨2702:TESITT⟩2.0.CO;2

Tobin, I., Bony, S., Holloway, C. E., Grandpeix, J.-Y., Sèze, G., Coppin, D., et al. (2013). Does convective aggregation need to be represented in cumulus parameterizations? *Journal of Advances in Modeling Earth Systems*, *5*(4), 692–703. https://doi.org/10.1002/jame.20047

Tselioudis, G., Tromeur, E., Rossow, W. B., & Zerefos, C. S. (2010). Decadal changes in tropical convection suggest effects on stratospheric water vapor. *Geophysical Research Letters*, *37*(14). https://doi.org/10.1029/2010GL044092

Watanabe, M., Kang, S. M., Collins, M., Hwang, Y.-T., McGregor, S., & Stuecker, M. F. (2024). Possible shift in controls of the tropical Pacific surface warming pattern. *Nature*, *630*(8016), 315–324. https://doi.org/10.1038/s41586-024-07452-7

Wheeler, M., & Kiladis, G. N. (1999). Convectively coupled equatorial waves: Analysis of clouds and temperature in the wavenumber–frequency domain. *Journal of the Atmospheric Sciences*, *56*, 374–399. https://doi.org/10.1175/1520-0469(1999)056⟨0374:CCEWAO⟩2.0.CO;2

Williams, A. I. L., Jeevanjee, N., & Bloch-Johnson, J. (2023). Circus tents, convective thresholds, and the non-linear climate response to tropical SSTS. *Geophysical Research Letters*, *50*(6), e2022GL101499. https://doi.org/10.1029/2022GL101499

Wills, R. C. J., Dong, Y., Proistosecu, C., Armour, K. C., & Battisti, D. S. (2022). Systematic climate model biases in the large-scale patterns of recent sea-surface temperature and sea-level pressure change. *Geophysical Research Letters*, *49*(17), e2022GL100011. https://doi.org/10.1029/2022gl100011

Wing, A. A., Emanuel, K., Holloway, C. E., & Muller, C. (2018). Convective self-aggregation in numerical simulations: A review. In R. Pincus, D. Winker, S. Bony, & B. Stevens (Eds.), *Shallow clouds, water vapor, circulation, and climate sensitivity* (pp. 1–25). Springer International Publishing. https://doi.org/10.1007/978-3-319-77273-8_1

Wing, A. A., & Emanuel, K. A. (2014). Physical mechanisms controlling self-aggregation of convection in idealized numerical modeling simulations. *Journal of Advances in Modeling Earth Systems*, *6*(1), 59–74. https://doi.org/10.1002/2013MS000269

Wodzicki, K. R., & Rapp, A. D. (2016). Long-term characterization of the Pacific ITCZ using TRMM, GPCP, and era-interim. *Journal of Geophysical Research: Atmospheres*, *121*(7), 3153–3170. https://doi.org/10.1002/2015JD024458

Wood, R., & Bretherton, C. S. (2006). On the relationship between stratiform low cloud cover and lower-tropospheric stability. *Journal of Climate*, *19*(24), 6425–6432. https://doi.org/10.1175/JCLI3988.1

World Data Center for Climate. (2023). Ifs_9–fesom_5 nextgems cycle 2 model output [Dataset]. https://doi.org/10.26050/WDCC/nextGEMS_cyc2

Young, A. H., Knapp, K. R., Inamdar, A., Hankins, W., & Rossow, W. B. (2018). The international satellite cloud climatology project h-series climate data record product. *Earth System Science Data*, *10*(1), 583–593. https://doi.org/10.5194/essd-10-583-2018

Zelinka, M. D., Myers, T. A., McCoy, D. T., Po-Chedley, S., Caldwell, P. M., Ceppi, P., et al. (2020). Causes of higher climate sensitivity in CMIP6 models. *Geophysical Research Letters*, *47*(1), e2019GL085782. https://doi.org/10.1029/2019GL085782